

Scaling Analysis of Temperature and Liquid Water Content in the Marine Boundary Layer Clouds during POST

YONG-FENG MA, SZYMON P. MALINOWSKI, AND KATARZYNA KARPIŃSKA

Faculty of Physics, Institute of Geophysics, University of Warsaw, Warsaw, Poland

HERMANN E. GERBER

Gerber Scientific Inc., Reston, Virginia

WOJCIECH KUMALA

Faculty of Physics, Institute of Geophysics, University of Warsaw, Warsaw, Poland

(Manuscript received 17 January 2017, in final form 28 August 2017)

ABSTRACT

The authors have analyzed the scaling behavior of marine boundary layer (MBL) clouds using high-resolution temperature (T) and liquid water content (LWC) fluctuations from aircraft measurements collected over the Pacific Ocean during the Physics of Stratocumulus Top (POST) research campaign in summer of 2008. As an extension of the past studies for scale-invariant properties of MBL clouds, the authors studied the variability of scaling exponents with height. The results showed that both LWC and T have two distinct scaling regimes: the first one displays scale invariance over a range from about 1–5 m to at least 7 km, and the second one goes from about 0.1–1 to 1–5 m. For the large-scale regime ($r > 1$ –5 m), turbulence in MBL clouds is multifractal, while scale break and scaling exponents vary with height, most significantly in the cloud-top region. For example, LWC spectral exponent β increases from 1.42 at cloud base to 1.58 at cloud top, while scale break decreases from ~ 5 m at cloud base to 0.8 m at cloud top. The bifractal parameters (H_1 , C_1) for LWC increase from (0.14, 0.02) at cloud base to (0.33, 0.1) at cloud top while maintaining a statistically significant linear relationship $C_1 \approx 0.4H_1 - 0.04$ in MBL clouds. From near surface to cloud top, (H_1 , C_1) for T also increase with height, but above cloud top H_1 increases and C_1 decreases with height. The results suggest the existence of three turbulence regimes: near the surface, in the middle of the boundary layer, and in the cloud-top region, which need to be distinguished.

1. Introduction

Patterns of marine boundary layer (MBL) clouds vary on spatial scales (Pierrehumbert 1996; Wood 2012), affecting the planetary albedo (Cahalan 1994) and strongly impacting Earth's radiation budget (Ramanathan et al. 1989; Wood 2012), which results in uncertainties of climate modeling results (Cess et al. 1989; Stanfield et al. 2014). This variability also affects the retrieval of cloud properties from remotely sensed data (Davis et al. 1997). Therefore, improvements in understanding the structure and variability of MBL clouds are very important and necessary.

Scaling analysis is a well-established method for describing the variability of atmospheric parameters

(Davis et al. 1996a). In the past several decades, numerous studies have presented the scaling behavior of selected atmospheric variables in the troposphere (e.g., Davis et al. 1994, 1996b, 1999; Marshak et al. 1997; Cho et al. 1999; Berton 2008; Fischer et al. 2013). However, only a few studies investigated the scale invariance of MBL clouds using aircraft in situ measurements. Malinowski et al. (1994) analyzed the fractal properties of cloud structure. Davis et al. (1996b) and Marshak et al. (1997) described the behavior of power spectrum and structure function of liquid water content (LWC) in marine stratocumulus clouds (MSC) by in situ airborne measurements during First ISCCP Research Experiment (FIRE I; Albrecht et al. 1988) over the Pacific Ocean and the Atlantic Stratocumulus Transition Experiment (ASTEX; also called FIRE II; Albrecht et al. 1995)

Corresponding author: Yong-Feng Ma, yfma@fuw.edu.pl

DOI: 10.1175/JAS-D-17-0015.1

© 2017 American Meteorological Society. For information regarding reuse of this content and general copyright information, consult the [AMS Copyright Policy \(www.ametsoc.org/PUBSReuseLicenses\)](http://www.ametsoc.org/PUBSReuseLicenses).

over the Atlantic Ocean. They found that the internal structure of MSC is multifractal over at least three decades in scale, from tens of meters to tens of kilometers. [Davis et al. \(1999\)](#) analyzed the horizontal structure of MBL clouds during the Southern Ocean Cloud Experiment (SOCEX; [Boers et al. 1996](#)) off the western coast of Tasmania and found that the LWC spectra exhibit two distinct scaling regimes: from 5 m to at least 2 km and from 8 cm to 2–5 m. These studies also found that the multifractal properties of MSC from different field experiments (FIRE, ASTEX, and SOCEX) are remarkably similar, suggesting that the cloud internal structure in the MBL depends mainly on the dynamics of cloud, rather than on the local climatology ([Marshak et al. 1997](#); [Davis et al. 1999](#)).

It has to be mentioned that the data analyzed in the above studies mainly focus on single-level horizontal legs within the stratocumulus (Sc) cloud layer and do not provide information on the vertical structure of the stratocumulus-topped boundary layer (STBL). However, it has already been established that the STBL has a complex vertical structure ([Wood 2012](#)). The typical structure of STBL is sketched in [Fig. 1](#). [Malinowski et al. \(2013\)](#) and [Jen-La Plante et al. \(2016\)](#) separated the STBL top region into four distinct sublayers: 1) free troposphere (FT), stably stratified and mostly nonturbulent; 2) turbulent inversion sublayer (TISL), with strong inversion characterized by increased static stability, marginally turbulent; 3) cloud-top mixing sublayer (CTMSL), also statically stable but with stability weaker than that of TISL, and the most turbulent sublayer of the STBL top region—turbulence in both TISL and CTMSL is produced by wind shear and usually anisotropic; and 4) cloud-top layer (CTL), a well-mixed layer with isotropic, strong turbulence. Therefore, taking into account the differences of thermodynamic and turbulent properties in these sublayers, it is important and necessary to analyze the scaling behavior at the cloud-top region.

In this study, we investigate the scaling properties of temperature (T) and LWC at different altitudes within STBL. Our analysis is based on the aircraft measurements collected from the Physics of Stratocumulus Top (POST) field campaign. It was performed in 2008 over the Pacific Ocean and collected a large dataset from horizontal segments within STBL and vertical segments (porpoises) across the cloud-top region ([Gerber et al. 2010, 2013](#); [Carman et al. 2012](#); [Malinowski et al. 2013](#)). The paper is structured as follows: In [section 2](#) we present information on the POST dataset and processing methods. In [section 3](#), we analyze first the scaling properties at different altitudes (near the sea surface, at cloud base, at cloud top, and in the free atmosphere) using horizontal segments (see [sections 3a](#) and [3b](#)) and

analyze second the properties in different sublayers within STBL using porpoise-like segments and the layer division algorithm developed by [Malinowski et al. \(2013\)](#) (see [sections 3c](#) and [3d](#)). In [section 4](#), we discuss the vertical distribution of the scaling exponents using the results from [section 3](#). In addition, the bifractal properties of T and LWC fluctuations in STBL and MSC are analyzed in [section 4b](#). We conclude in [section 5](#). [Appendix A](#) is a list of abbreviations and acronyms; [Appendix B](#) is a listing of the layers grouped from horizontal segments used in the study; [appendix C](#) gives the sublayers in the cloud-top region grouped from porpoises; and [appendix D](#) is a list of all the parameters in this study.

2. Data and methods

a. Data description

We use high-resolution airborne in situ measurements from the POST research campaign held in July–August 2008 in the vicinity of Monterey Bay ([Gerber et al. 2010, 2013](#); [Carman et al. 2012](#); [Malinowski et al. 2013](#)). The CIRPAS Twin Otter (TO) research aircraft carried the modified UltraFast Thermometer (UFT-M; [Kumala et al. 2013](#)) and the Particulate Volume Monitor PVM-100A ([Gerber et al. 1994](#)) to sample T and LWC at 1000-Hz frequency, which corresponds to ~ 5.5 -cm spatial resolution at $\sim 55 \text{ m s}^{-1}$ true airspeed of the aircraft. Every flight was composed of several horizontal segments at different altitudes connected by steep climbs and descents, as well as many porpoise-like segments across the cloud top [see the schematic trajectory in [Fig. 1](#) and the real trajectory in [Fig. 3](#) of [Gerber et al. \(2010\)](#)]. We focus on the horizontal segments between 12.7 and 52.2 km long that were flown near the sea surface [herein hNS; usually at ~ 30 – 50 m above sea level], at the cloud base (hCB), in the cloud close to the cloud top (hCT), and in the free atmosphere above the cloud top (hFA); see [Fig. 1](#). [Davis et al. \(1999\)](#) defined an in-cloud segment as one with at least 60% data points of $\text{LWC} \geq 0.02 \text{ g m}^{-3}$. We calculate such a percentage for every segment and found that it is distinctly different for our layer categories. The percentage is close to 0% for the segments near sea surface (hNS) and free atmosphere (hFA), $\sim 10\%$ – 30% for the segments near cloud base (hCB) with mean $\text{LWC} < 0.15 \text{ g m}^{-3}$, and $\sim 94\%$ – 100% for the segments near cloud top (hCT) with mean LWC usually $> 0.25 \text{ g m}^{-3}$. Data from 67 individual horizontal segments of total ~ 2850 -km length collected in six flights (TO03, TO05, TO10, TO12, TO13, and TO14) were analyzed. The information on horizontal segments and statistical properties of T and LWC are listed in [Table 1](#). More detail of environmental conditions for the POST

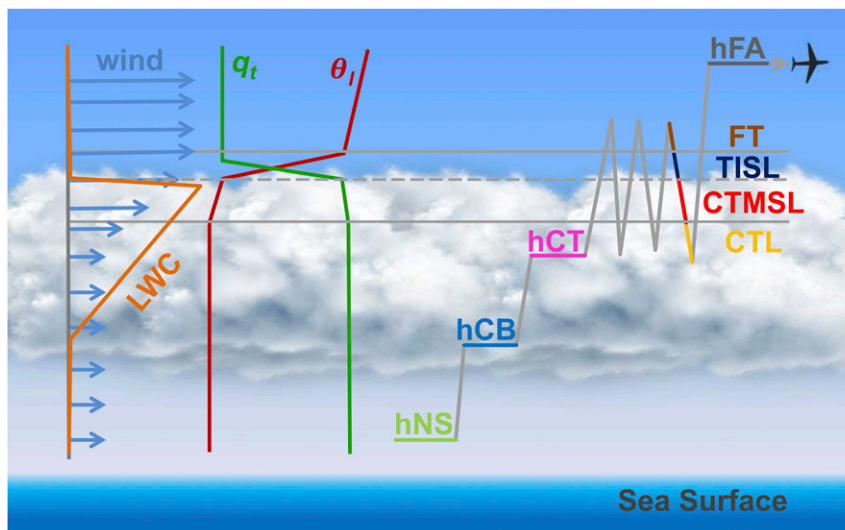


FIG. 1. A sketch of flight pattern, layer division, and vertical profiles of total water mixing ratio (q_t), liquid water potential temperature (θ_l), LWC, and winds of marine stratocumulus clouds during POST. All layers (hNS, hCB, hCT, and hFA) are grouped from horizontal flight segments and all sublayers of the cloud-top region (FT, TISL, CTMSL, and CTL) categorized from porpoise-like segments are marked on the flight trajectory. The layer between two horizontal solid gray lines is the EIL, which is the combination of TISL and CTMSL. Below FT is the STBL.

flights can be seen in Table 1 of Gerber et al. (2013) and Table 1 of Jen-La Plante et al. (2016).

To get the scaling properties in the cloud-top region, we also processed all the porpoise-like segments (more than 200) through the cloud top using the layer division algorithm (Malinowski et al. 2013; Jen-La Plante et al. 2016). This method identifies the vertical divisions between the stable FT above the cloud, the TISL characterized by temperature inversion and wind shear, a moist and sheared CTMSL, and the well-mixed CTL. The layer division method is summarized as follows: 1) the division between the FT and TISL is identified by the highest point where the gradient of liquid water potential temperature exceeds 0.2 K m^{-1} and turbulence kinetic energy (TKE) exceeds $0.01 \text{ m}^2 \text{ s}^{-2}$, 2) the division between the TISL and CTMSL is determined by the uppermost point where $\text{LWC} > 0.05 \text{ g m}^{-3}$, and

3) the division between the CTMSL and CTL is identified by the point at which the square of the horizontal wind shear reaches 90% of the maximum. The sketch of layer division of the MSC top region is shown in Fig. 1 [the division on the real flight trajectory can be seen in Fig. 1 of Jen-La Plante et al. (2016)], with sublayers from top to bottom shown as FT, TISL, CTMSL, and CTL, where TISL and CTMSL compose the entrainment interfacial layer (EIL). The averaged cloud-top height is about $566 \pm 106 \text{ m}$, and the cloud thickness is about $323 \pm 74 \text{ m}$. The thicknesses of TISL and CTMSL respectively are in the ranges of 14–35 and 25–75 m, with mean values of 23 ± 7 and $50 \pm 19 \text{ m}$.

b. Methods of scaling analysis

We take the methods proposed by Davis et al. (1994, 1996b, 1999) and Marshak et al. (1997) and use them on

TABLE 1. Characteristics and statistical properties of high-resolution T and LWC datasets from the POST campaign: N is the number of individual horizontal flight segments (for LWC, $N = 13$ at hCB); N_p is total number of sampling points; L_t is total length of the segments. Standard deviation of altitude (z), T , and LWC are also shown in the table.

Layer	N	N_p (points)	L_t (km)	z (m)	T ($^{\circ}\text{C}$)	LWC (g m^{-3})
hFA	5	2 585 907	142.1	925 ± 313	22.2 ± 3.1	0
hCT	20	13 909 633	765.0	464 ± 116	10.6 ± 0.9	0.312 ± 0.102
hCB	22	21 098 542	1158.2	265 ± 116	11.7 ± 1.4	0.139 ± 0.127
hNS	20	14 187 958	781.6	49 ± 30	13.7 ± 0.7	0

the POST dataset. The power spectrum and structure function are calculated to analyze the scaling characteristics of T and LWC field. In the layers hNS, hCB, hCT, and hFA we use horizontal segments. In the sublayers (FT, TISL, CTMSL, and CTL) of cloud-top region, we use layer division adopted to the porpoise-like segments. All the time series data are converted into spatial distributions according to the Taylor's frozen turbulence hypothesis with an assumption of constant aircraft speed (55 m s^{-1}).

1) POWER SPECTRUM

As described by Davis et al. (1996b) and Marshak et al. (1997), the power spectrum follows a power law under an assumption that the field is scale invariant:

$$E(f) \propto f^{-\beta}, \quad (1)$$

where $E(f)$ is power spectrum, f is frequency, and β is the spectral exponent. A condition of $\beta < 1$ implies that the process is stationary and $1 < \beta < 3$ implies that the process is nonstationary with stationary increments (Davis et al. 1996b).

To get a representative scaling range and spectral exponent of the power law, as Davis et al. (1999) did, we separate all the longer segments into several independent nonoverlapping subsegments (the length determined by the shortest segment available), and calculate power spectra using fast Fourier transform (FFT) for all these subsegments, then obtain the aggregated spectra for each layer. In this study, all horizontal (vertical) segments are processed according to the subdivision method with $N_p = 2^{17}$ ($N_p = 2^{11}$) points (2 to the power of the integer of $\log_2 N_{ps}$, where N_{ps} is number of sampling points of the shortest segment), corresponding to the horizontal length $\sim 7.2 \text{ km}$ ($\sim 112.6 \text{ m}$). Thus, the upper limit of the large-scale range can only reach 7.2 km for horizontal segments and 112.6 m for porpoise-like segments, losing some information on the scales larger than these upper limits.

2) STRUCTURE FUNCTION

The one-dimensional q th-order horizontal structure function is defined by

$$S_q(r) = \langle |f(x+r) - f(x)|^q \rangle, \quad 0 \leq r \leq L, \quad (2)$$

$$0 \leq x \leq L - r,$$

where $f(x)$ is a one-dimensional signal (such as T and LWC), r is some finite difference in x , $\langle \cdot \rangle$ denotes an ensemble mean, and L is the length of horizontal segment.

Under the assumption of scale invariance and $1 < \beta < 3$ (nonstationary with stationary increments), the q th-order structure function scales with r and can be written as

$$S_q(r) \propto r^{\zeta(q)}, \quad (3)$$

where $\zeta(q)$ is a scaling exponent. If $\zeta(q)/q$ is a constant, the relation is called ordinary scaling or monofractal (or monoscaling), while nonconstant $\zeta(q)/q$ denotes anomalous scaling or multifractal (or multiscaling). The $\zeta(q)$ function can be used to describe intermittency with the larger deviations from linear scaling indicating increased intermittency (Pierrehumbert 1996). To estimate the intermittency an empirical multifractal formula introduced by Pierrehumbert (1996),

$$\zeta(q) = \frac{aq}{1 + aq/\zeta_\infty}, \quad (4)$$

where $a \in [0, \infty]$ measures the average level of fluctuations and $\zeta_\infty \in (0, \infty]$ measures the degree of multifractality, with decreasing values corresponding to higher intermittency. The parameter a and ζ_∞ can be fitted from $q - \zeta(q)$ curve by Eq. (4).

3) ESTIMATION OF SCALE BREAK AND SCALING EXPONENT

Most often scaling exponents of atmospheric datasets estimated from power spectra (e.g., Davis et al. 1994, 1999; Kahn et al. 2011) or structure function (e.g., Pierrehumbert 1996; Marshak et al. 1997; Cho et al. 2000; Tuck 2010; Fischer et al. 2013) are determined by linear regression in log-log space because this approach is easy to implement and automate. We also use linear least squares method (LSM) in log-log space to estimate the scaling exponents for simplicity and consistency with the literature.

To reduce the noise, all raw spectra were averaged over equidistant logarithmic frequency bins (f_{bins}). The total number of bins depends on the length of each segment and the bin resolution n . In this study we use $n = 50$; that is, there are 50 f_{bins} between $f = 10^m \text{ Hz}$ and $f = 10^{m+1} \text{ Hz}$ (m is an integer) in the log-log plot. After bin averaging, we first look for the scale break of the spectrum, which is defined as a scale below which the spectrum no longer follows the same power law. We repeat linear regression between 0.3 Hz and all $f_{\text{bins}} > 5 \text{ Hz}$ in log-log space and define the position where the linear fitting coefficient of determination (R^2) reaches the maximum and $R^2 \geq 0.95$ as the scale break point. Second, we perform linear LSM on the bin-averaged spectra in log-log space to get the scaling exponent β . Next a one-tailed t test is used to compute the 95%

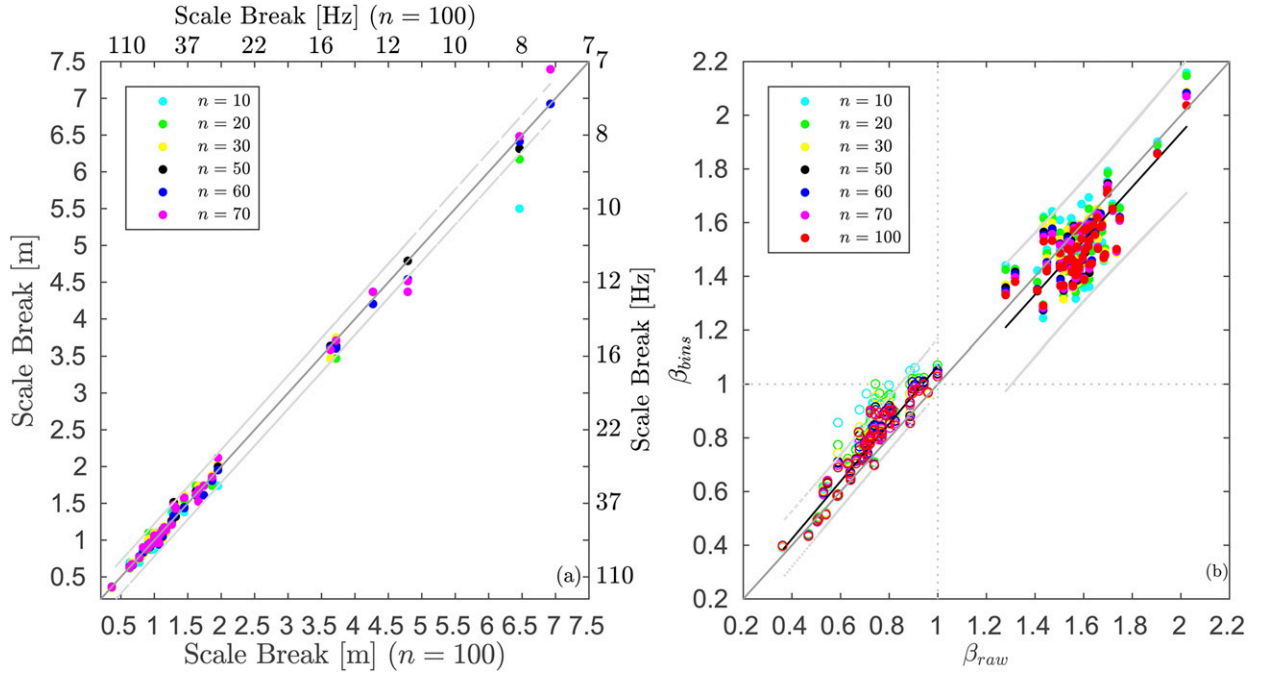


FIG. 2. (a) Comparison of scale breaks at different f_{bins} resolution n . The gray dashed lines are 95% confidence intervals of the linear fit between $n = 70$ and $n = 100$. (b) Comparison of β estimated from bin-averaged spectra (β_{bins}) and from raw spectra (β_{raw}). The solid circles are for the large scales and the circles with clear centers are for the small scales. The black solid lines are linear fits for $n = 100$ and the gray lines are their 95% confidence intervals.

confidence intervals of β and its uncertainty is estimated at the 95% confidence level: that is, $\Delta\beta = t^*(S/N^{1/2})$, where t^* is the upper $(1 - \alpha)/2$ critical value for the t distribution $t(N - 1)$ with $N - 1$ degrees of freedom and $S/N^{1/2}$ is standard deviation. For other scaling parameters estimated by the fitting procedure, we also use the same method to estimate the uncertainty. The uncertainty of the scale break is estimated from the adjacent f_{bins} of break point: that is, if the bin-averaged power spectrum breaks at $f_{\text{bins}} = 10^{m+i/n}$ Hz ($i = 1, 2, \dots, n$), the uncertainty of scale break is $(1/2)[\{U/10^{m+(i+1)/n}\} - \{U/10^{m+(i-1)/n}\}]$ m at $U \simeq 55 \text{ ms}^{-1}$ mean true airspeed.

To study the impact of f_{bins} resolution n on the scale break and scaling exponent, we test $n = 10, 20, 30, 50, 60, 70$, and 100 for T from all 67 individual horizontal segments. Figure 2a shows a comparison of the scale break estimated in different n . The differences of the spatial scale break between $n < 100$ and $n = 100$ are large (~ 1 m) [small (< 0.2 m)] when the power law breaks at lower ($f < 10$ Hz) [higher ($f > 30$ Hz)] frequencies, with the absolute mean biases and root-mean-square errors (RMSE) in the ranges of 0.01 – 0.03 and 0.05 – 0.13 m, respectively. In our cases, about 90% of the spectra of T breaks at 0.6 – 2 m (27–90 Hz), resulting in a small influence on the spatial scale break

from f_{bins} resolution n , especially when $n > 20$. Figure 2b shows a comparison of the scaling exponent estimated from bin-averaged spectra (β_{bins}) and from raw spectra (β_{raw}). The values of β_{bins} for the large scale ($1 < \beta < 3$) are slightly smaller than β_{raw} , with fitted slopes and mean biases of the comparison between β_{bins} and β_{raw} in the ranges from 0.97 to 1.0 and -0.07 to -0.04 , respectively. This feature is similar to the results in Davis et al. (1996b). For the MBL T , we get the mean values are $\langle \beta_{\text{raw}} \rangle = 1.59 \pm 0.12$ and $\langle \beta_{\text{bins}} \rangle = 1.53 \pm 0.12$, with the corresponding median values 1.58 and 1.47 . The values of β_{bins} for the small scale ($0 < \beta < 1$) are slightly larger than β_{raw} , with fitted slopes and mean biases of the comparison between β_{bins} and β_{raw} in the ranges of 1.09 – 1.17 and 0.05 – 0.09 , respectively. In the MBL, the mean values are $\langle \beta_{\text{raw}} \rangle = 0.77 \pm 0.19$ and $\langle \beta_{\text{bins}} \rangle = 0.82 \pm 0.20$, with the corresponding median values 0.74 and 0.81 . Figure 2b also shows the values of β are not sensitive to n , especially when $n > 20$, because the power spectra follow a power law very well in our cases.

In addition, we use nonlinear regression to estimate the scaling exponents from spectra. However, it cannot get correct values for all cases (not shown here) because of its sensitivity to the initial values and weight function for robust fitting. In such cases, it is not easy to

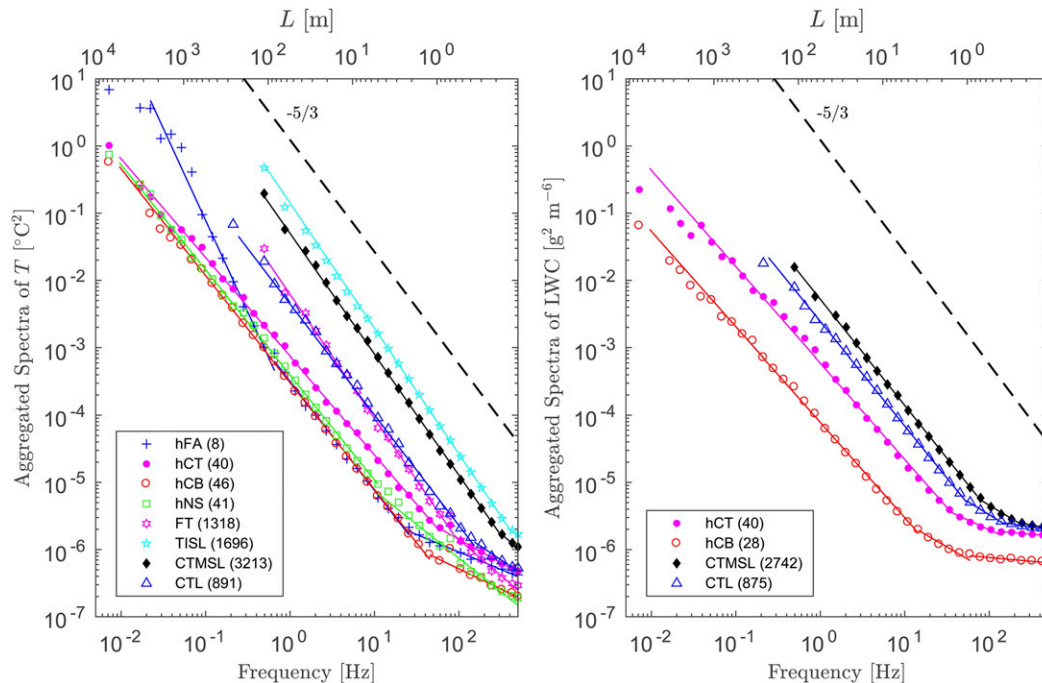


FIG. 3. Aggregated spectra of (left) T and (right) LWC fluctuations for different layers/sublayers from six flights during POST. The black dashed bold line is $-5/3$ slope and the solid lines are fitted slopes of each scaling regime for each layer. The numbers in the parentheses are the total number of subsegments used for each layer. Each subsegment has 2^{17} sampling points (~ 7.2 km) for layers hFA, hCT, hCB, and hNS; and 2^{11} sampling points (~ 112.6 m) for sublayers FT, TISL, CTMSL, and CTL.

automate batch processing. Thus, for convenience and safety we recommend using linear regression in log–log space rather than a complex nonlinear regression, at least for the POST datasets.

3. Results

a. Scaling analysis of horizontal segments at different altitudes

1) POWER SPECTRA ANALYSIS

Compared with the $-5/3$ scaling law, the spectra of T and LWC for all horizontal segments roughly follow the $-5/3$ power law until the frequency increases to ~ 10 – 100 Hz, which corresponds to ~ 0.5 – 5 m, depending on the segment, flight, and variable. At higher frequencies there exists a “scale break” and after that the spectrum follows a different power law. Figure 3 shows the aggregated spectra of T and LWC for different layers from six flights (the information on horizontal segments and total number of subsegments we used are listed in Table 1 and Table 2). It shows that both T and LWC fluctuations at different altitudes within the STBL have two distinct scaling regimes

(a wide large scale and a narrow small scale), similar to the scaling behavior of LWC in stratocumulus/cumulus (Cu) clouds in Davis et al. (1996b, 1999) and Gerber et al. (2001). This scale break suggests that different physical processes dominate each scaling regime (Davis et al. 1999). The first scaling regime is presumably dominated by turbulence dynamics in the inertial subrange, but the second scaling regime is still poorly understood. Davis et al. (1999) and Gerber et al. (2001) demonstrated that instrument limitation is insufficient to explain the enhanced variance at small scales; thus, the second scaling regime is likely to be physical. This scale break and different scaling regime at small scales may be related to the injection of a new energy source, like entrainment of drier and more energetic environmental air into the clouds (Gerber et al. 2001), or due to buoyancy production at small scales in the course of cloud and clear air mixing (Malinowski et al. 2008).

We calculated the spectral exponents and scale ranges of both scaling regimes of T and LWC for each layer; see Table 2. For cloud-top LWC, the large scale is in the range of 1.7 ± 0.1 m– 7.2 km with $\beta_L = 1.43 \pm 0.02$, and the small scale is in the range of 0.5 ± 0.05 m– 1.7 ± 0.1 m with $\beta_S = 0.58 \pm 0.04$. For LWC near cloud base, the

TABLE 2. Spectral exponent (β) and the corresponding scale range (SR) of T and LWC at different layers during POST. The quantity N_{sub} is the number of independent nonoverlapping subsegments separated from N horizontal segments (Table 1), with 2^{17} sampling points (~ 7.2 km in length). For LWC, $N_{\text{sub}} = 28$ at hCB. The subscripts L and S are respectively for the large-scale and small-scale regime. For comparison with other MSC, we added the corresponding values in ASTEX, FIRE, SOCEX, and ECRIN96 experiments from literature. The resolution (longest) segment for ASTEX, FIRE, and SOCEX are 5 m (131 km), 8 m (328 km), and 4 cm (26 km), respectively. For the details of these datasets and scaling analysis, see footnotes.

Layer	N_{sub}	Scaling regimes of T				Scaling regimes of LWC			
		SR _L	β_L	SR _S	β_S	SR _L	β_L	SR _S	β_S
hFA	8	94.3 \pm 2.2 m–2.7 km	2.73 \pm 0.12						
		2.2 \pm 0.1 m–94.3 m	1.62 \pm 0.03	0.1–2.2 m	0.53 \pm 0.06				
hCT	40	0.95 \pm 0.05 m–7.2 km	1.47 \pm 0.01	0.1–0.9 m	0.75 \pm 0.07	1.7 \pm 0.1 m–7.2 km	1.43 \pm 0.02	0.5 \pm 0.05–1.7 m	0.58 \pm 0.04
hCB	46	1.5 \pm 0.1 m–7.2 km	1.59 \pm 0.01	0.1–1.5 m	0.62 \pm 0.07	5.0 \pm 0.25 m–7.2 km	1.42 \pm 0.02	1.06 \pm 0.05–5.0 m	0.73 \pm 0.04
hNS	41	5.2 \pm 0.2 m–7.2 km	1.56 \pm 0.01	0.1–5.2 m	1.02 \pm 0.04				
ASTEX ^a						60 m to 60 km	1.43		
FIRE ^a						20–40 m to 20 km	1.36		~ 0.7
SOCEX ^b						2–5 m to 5–10 km	1.6 \pm 0.1	8–16 cm to 2–5 m	0.9 \pm 0.1
ECRIN96 ^c		~ 50 m–10 km	1.32			~ 50 m to 10 km	1.11		

^a Davis et al. (1996b).

^b Davis et al. (1999).

^c Berton (2008).

large scale is in the range of 5 ± 0.25 m–7.2 km with $\beta_L = 1.42 \pm 0.02$ and the small scale is in the range of 1.06 ± 0.05 m– 5 ± 0.25 m with $\beta_S = 0.73 \pm 0.04$. The values of β_L are similar to 1.41–1.45 for MBL water vapor during the Variability of the American Monsoon Systems Ocean-Cloud-Atmosphere-Land Study Regional Experiment (VOCALS-REx; Kahn et al. 2011). By comparison to other MSC experiments (see Table 2), we may see that β_L of LWC in POST MSC is similar to that in ASTEX ($\beta_L = 1.36$) and FIRE ($\beta_L = 1.43$) (Davis et al. 1996b) and not far from that in SOCEX ($\beta_L = 1.6$). This implies that to a certain extent, the thermo-hydrodynamic processes are universal in the MSC under different local climatological conditions. The scale ranges of LWC in POST MSC are similar to that in SOCEX (from 8–16 cm to 2–5 m for small scales and from 5 m to 5–10 km for large scales). However, the upper limit of scale range of large scale (SR_L) is smaller than that in ASTEX (60 km) and FIRE (20 km) (Davis et al. 1999), because it may be mainly determined by the maximum segments' length and local atmospheric conditions [e.g., the thickness of the boundary layer (Marshak et al. 1997)]. In this study the longest horizontal segment is ~ 50 km, which is much shorter than 131 km in ASTEX and 328 km in FIRE (Davis et al. 1999); and the average thickness of MBL during POST is ~ 590 m, which is less than ~ 1500 m in ASTEX (Marshak et al. 1997). If we just analyze the longest individual horizontal segment at cloud base of POST data, the upper limit of SR_L can increase to ~ 14.5 km.

For cloud temperature, the scaling regimes are similar to that of LWC, but the values of β_L are a little larger while the lower limit of the scale range reaches to a smaller scale [~ 1 m for SR_L and ~ 0.1 m for SR_S (scale range of small scale)]; see Table 2. Our results for β_L (1.47 for cloud top and 1.59 for cloud base) are slightly larger than 1.3–1.35 in the ECRIN96 Experiment Sc (Berton 2008) and 1.41–1.43 in the VOCALS-REx Sc (Kahn et al. 2011), and SR_L is similar to that in the ECRIN96 (about 50 m–10 km) and VOCALS-REx (< 10 km). Near the sea surface T fluctuations show a large-scale regime in the range of 5 m–7 km with $\beta_L = 1.56 \pm 0.01$, which is in agreement with the universal scaling exponent $\beta = 1.55$ for global near-surface temperature obtained from reanalysis datasets (Fallah et al. 2016). The small-scale regime falls in the range of 0.1–5 m with $\beta_S = 1.02 \pm 0.04$, which is larger than that at other layers, suggesting more temperature variance in the surface layer. This f^{-1} scaling law for T fluctuations at small scales most likely indicates the viscous-convective subrange (e.g., Gibson and Schwarz 1963; Hill 1989), which was first predicted by Batchelor (1959) and has been confirmed to exist for

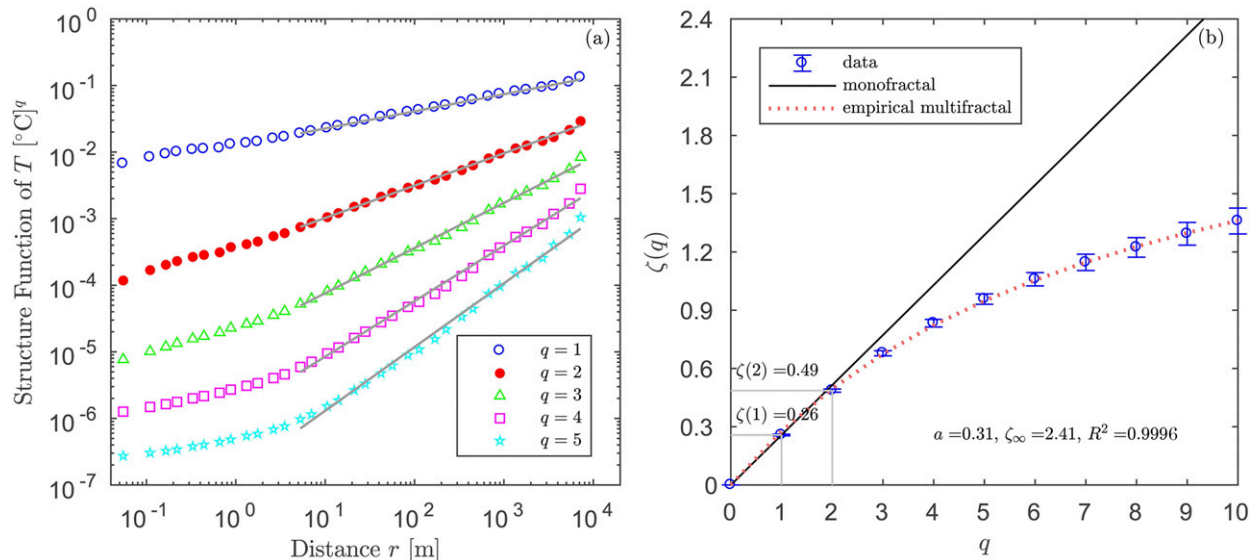


FIG. 4. Structure function analysis for temperature near the sea surface (the mean height is ~ 50 m). (a) Aggregated structure function calculated up to the tenth order (we only show up to the fifth order for visual clarity) from 41 independent nonoverlapping subsegments 7.2 km in length. Straight lines are log–log linear least squares fits from $r = 5.2$ m to $r = 7.2$ km. (b) Large-scale exponents $\zeta(q)$ calculated from the linear fits in (a) vs the order q . Two important exponents are emphasized at $q = 1, 2$. The black line is $q\zeta(1)$, indicating monofractal. The pink dashed line is fitted by the empirical multifractal formula [Eq. (4)], and the fitted parameters are shown at the bottom.

passive scalars in laboratory experiment (Gibson and Schwarz 1963), in the atmosphere (e.g., Willis and Deardorff 1974; Jeffery 2001), and in the ocean (e.g., Grant et al. 1968; Smyth and Moum 2009). In the viscous–convective subrange, the scales are not small enough for the thermal diffusivity to smear out the T fluctuations (Celani et al. 2005), and the spectra are dominated by molecular viscosity while the regime is actively convective (Kundu et al. 2008; Davidson et al. 2012). For the free atmosphere T fluctuations show three scaling regimes: the first regime in the range of 94.3 ± 2.2 m–2.7 km with $\beta = 2.73 \pm 0.12$ (close to 3) is likely associated with internal gravity waves (e.g., Riley and Lindborg 2008; Sukoriansky and Galperin 2013), the second regime is in the inertial subrange of turbulence in the range of 2.2 ± 0.1 m–94 m with $\beta = 1.62 \pm 0.03$ (close to $5/3$), and the third regime has $\beta = 0.53 \pm 0.06$ in a scale range of 0.1–2.2 m. The transition of spectra from the f^{-3} to $f^{-5/3}$ scaling law indicates that both wave motions (e.g., gravity waves or Kelvin–Helmholtz waves) and turbulence exist, and as the findings of Cho et al. (1999) showed it describes a general state of mixed wavelike motions and turbulence in the free atmosphere.

2) STRUCTURE FUNCTION ANALYSIS

We calculate structure function of T and LWC for orders from $q = 1$ to $q = 10$. Figure 4 shows an example

of aggregated structure function of T near the sea surface for six flights. As the spectra show, the structure function also clearly shows two distinct regimes with the same scale break around $r = 5.2$ m for all orders ($q = 6$ –10 are not shown). We calculate the log–log slopes $\zeta(q)$ by fitting a straight line between the scale break and the biggest r . For the large-scale regime, we get $\zeta(1) = 0.26$ and $\zeta(2) = 0.49$ using Eq. (3) and find that the value of $\zeta(2) + 1$ [which equals to β in regimes where $1 < \beta < 3$ based on the theory of Monin and Yaglom (1975)] agrees well with $\beta_L = 1.46$ estimated from Eq. (1). Figure 4b demonstrates a good fit of the empirical multifractal formula [Eq. (4)], with the curve obviously departing from monofractal scaling for $q \geq 2$. That indicates that the large-scale behavior of T near the sea surface is a multifractal and nonstationary process in the scale range from 5.2 m to 7.2 km. The fitted parameters in Fig. 4b are very close to that of MBL humidity variations from NASA’s Pacific Exploratory Mission in the Tropics (PEMT) over the tropical Pacific Ocean: $\zeta(1) = 0.25 \pm 0.02$, $\zeta(2) = 0.46 \pm 0.04$, $a = 0.29 \pm 0.03$, and $\zeta_\infty = 2.7 \pm 0.4$ (Cho et al. 2000). We suggest that this similar scaling regime reflects a universal structure of the MBL turbulence.

Table 3 shows the scaling parameters of T and LWC for all different layers calculated from the ensemble-averaged structure function from six flights. The parameter $\zeta(1)$ in the range of 0–1 characterizes the

TABLE 3. Statistical properties of structure function for horizontal segments grouped by different layers. For information about horizontal segments, see Table 1. For comparison with other MSC, we added the corresponding values of LWC in ASTEX, FIRE, and SOCEX from literature (see footnotes).

Layer	T			LWC		
	$\zeta(1)$	$\zeta(2)$	ζ_∞	$\zeta(1)$	$\zeta(2)$	ζ_∞
hFA	0.39 ± 0.06	0.84 ± 0.12	6.86 ± 0.69			
hCT	0.24 ± 0.003	0.45 ± 0.01	0.80 ± 0.10	0.16 ± 0.004	0.32 ± 0.02	0.79 ± 0.10
hCB	0.28 ± 0.003	0.51 ± 0.01	1.42 ± 0.11	0.12 ± 0.002	0.23 ± 0.004	0.92 ± 0.06
hNS	0.26 ± 0.004	0.49 ± 0.01	2.41 ± 0.09			
ASTEX ^{a,b}				0.29	0.48 ± 0.02	
FIRE ^b				0.28	0.37	
SOCEX ^c				0.31 ± 0.01	0.51 ± 0.02	

^a Davis et al. (1996b).

^b Marshak et al. (1997).

^c Davis et al. (1999).

nonstationarity of the data and is often called a Hurst exponent (H_1) (Marshak et al. 1997). It increases with the smoothness and nonstationarity of the investigated data series. From Table 3 we can see that T variations in the free atmosphere are less rough but more nonstationary than that in the cloud and near the sea surface. The LWC variations are more rough and stationary than T variations in the cloud. For LWC, values of $\zeta(1) = 0.16$ near cloud top and $\zeta(1) = 0.12$ near cloud base are significantly lower than $1/3$ obtained from Kolmogorov's classical turbulence theory and are also lower than that for other MSC experiments: 0.28 for FIRE, 0.29 for ASTEX (Marshak et al. 1997), and 0.25 for the MBL humidity in PEMT (Cho et al. 2000). The small values in POST are likely related to many strong down spikes in the LWC signals, which can make the values of $\zeta(1)$ and $\zeta(2)$ smaller (Marshak et al. 1997). In contrast, the values of $\zeta(1)$ for T in the STBL and MSC are closer to the theoretical value $1/3$. The values of $\zeta(2) + 1$ and β_L are similar but not identical (Table 2). In some cases, the differences are larger than 0.2 (e.g., at hFA for T and at hCB for LWC). This probably caused by the uncertainty of the fitting procedure and the consequence of nonstationarity and intermittency. All β fall between 1 and 3, which means the fluctuations of both T and LWC in the STBL are nonstationary with stationary increments.

We find that the smallest value of the intermittency parameter ζ_∞ appears at hCT for both T and LWC, implying that T and LWC fields are more intermittent close to the cloud top. At the free atmosphere, $\zeta_\infty = 6.9$ for temperature and it is obviously larger than that in STBL, given that the free-tropospheric variations are less intermittent (Cho et al. 2000). The values of parameters (a , ζ_∞) for the free-atmosphere temperature (0.48, 6.86) and near-surface temperature (0.31, 2.41) in POST are respectively similar to

(0.49, 4.7) for extratropical free-tropospheric humidity and (0.29, 2.7) for MBL humidity in PEMT (Cho et al. 2000).

3) EFFECTS OF MEASUREMENT ERRORS ON THE SCALING BEHAVIOR

To study the effect of measurement errors on the scaling behavior of T and LWC, series of random noises based on the level of measurement uncertainties are added to the observed signals using the Monte Carlo (MC) approach. Here, the uncertainty of the measurement for T is error = 0.01 K [the thermal resolution of UFT-M 1000-Hz data (Kumala et al. 2013)] and for LWC the uncertainty is 2% (the measurement precision of PVM-100A; see <http://www.gerberscience.com/pvmaspecs.html>) of the mean measured value (i.e., error = 2% \times obs) of each horizontal segment, which is in the range of 0.004–0.008 g m⁻³. We perform 100 MC “realization” simulations. In each MC simulation, we add random noises within plus-and-minus errors to the observational signals and calculate the power spectrum. We repeat this procedure 100 times then calculate the ensemble mean spectra of these 100 trials and estimate the scale break and β . Finally, we average the values estimated from 100 MC simulations.

We apply this calculation procedure to every horizontal segment. The mean β of 100 MC simulations ($\langle\beta_L\rangle$) for all horizontal segments are compared to that estimated from original measurements (β_{org}) in Fig. 5. We can see that the values of $\langle\beta_{\text{MC}}\rangle$ are very close to β_{org} , with a mean bias of -0.026 for T and -0.001 for LWC. The standard deviation of $\langle\beta_{\text{MC}}\rangle$ for individual segments are small, usually between 10^{-5} and 10^{-3} (not shown here). In comparison with Table 2, we get almost the same results for the large scale from MC simulations for both T and LWC. Only in some individual cases β_L decreases by 0.01 and the lower limit of SR_L increases

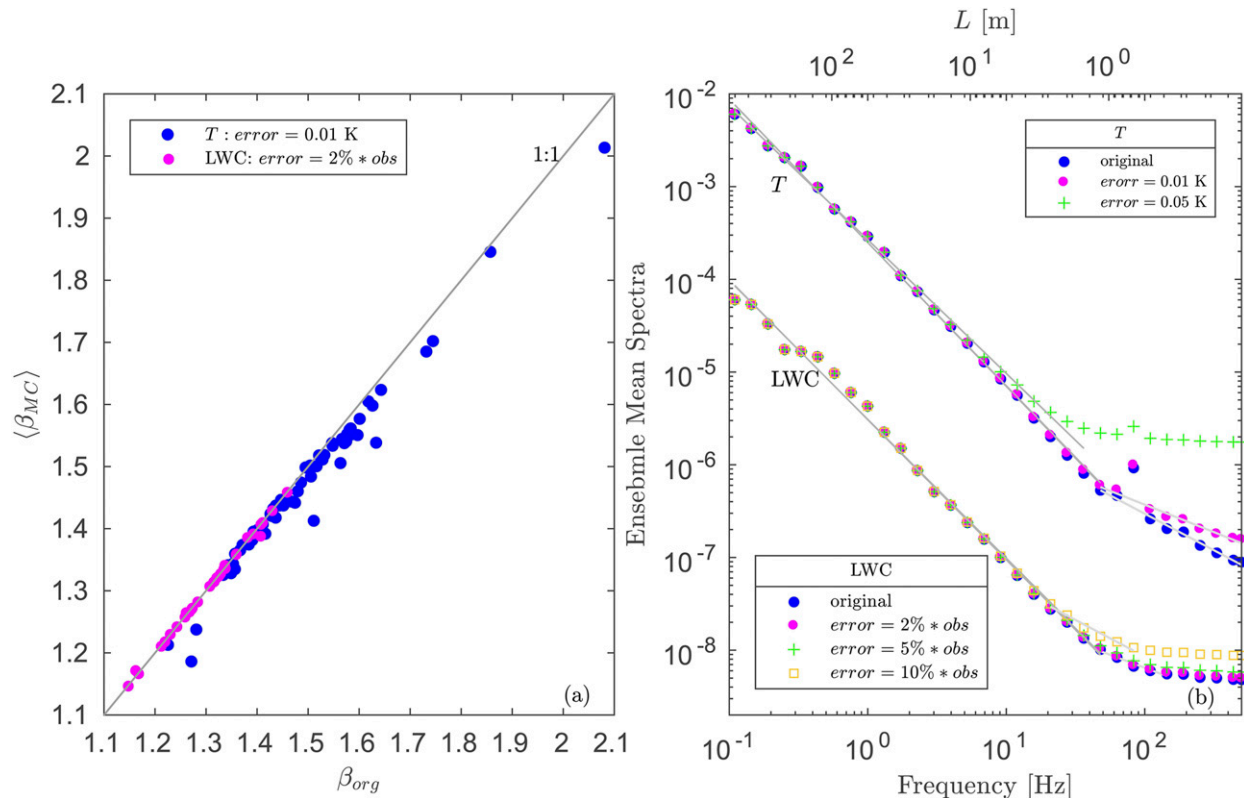


FIG. 5. (a) Comparison of averaged β (for large scale) of the 100 MC “realization” simulations ($\langle \beta_{MC} \rangle$) with that estimated from original measurements (β_{org}) for all horizontal segments. (b) Aggregated power spectra of the 100 MC simulations over different measurement error scenarios and that calculated from the original measurements for T and LWC at hCT layer in flight TO05. The straight lines are linear fits for different scaling regimes. For visual clarity, a part of large scale was cut off and the spectra of LWC were multiplied by 10^{-2} .

by 0.1 m. For the small scale, β_S becomes smaller and decreases by 0.06–0.12 at all layers. Therefore, the measurements errors (0.01 K for T and 2% of measured value for LWC) have a small influence on the scaling regime of the large scale and the errors can be neglected. Their influence on the small scales is more obvious (also see the spectra in Fig. 5b) than that on the large scales, but the effects are limited.

In addition, we tested larger measurement errors: 0.05 K for T ; 5% (~ 0.01 – 0.02 g m^{-3}) and 10% (~ 0.02 – 0.04 g m^{-3}) of the mean measured values for LWC. From Fig. 5b, we can see the larger measurement errors still have a small influence on β_L . Compared to the original spectra (β_L equals to 1.56 for T and 1.52 for LWC), β_L decreases by 0.1 for T with error = 0.05 K and decreases by 0.01 for LWC with error = $10\% \times \text{obs}$. However, the larger measurement errors have an obvious influence on the scale break and scaling regime of the small scale. When measurement error increases, the scale break point moves to a lower frequency and the small scales are almost dominated by the white noise;

that is, the atmospheric variability at small scales is weaker than the instrumental noise. Thus, only the high-resolution sensors with high precision can measure the structure of small scales. In addition, from the LWC spectra, we can see the small scale still can be measured even though the uncertainty of measurement reaches to 10% of the measured value. This confirms that the scale break and scaling regime of small scales is indeed a physical phenomenon rather than the results of the sampling errors (Davis et al. 1999; Gerber et al. 2001).

b. Scaling properties of MSC top region

The horizontal segments for the near-cloud-top layer (hCT) are slightly below the cloud top. To better understand the scaling properties of the cloud-top region, we use the layer division algorithms (Malinowski et al. 2013) to divide the cloud-top region into four sublayers (FT, TISL, CTMSL, and CTL) using the porpoise-like segments and then calculate the power spectrum and structure function and aggregate them in each sublayer. Each flight has about 50–60 porpoise-like segments

through the cloud-top region, of which ~ 30 – 50 porpoises can be successfully detected all sublayers by the layer division algorithms. Since some individual porpoises are too shallow, either division between TISL and FT or CTL and CTMSL cannot be detected. To avoid false estimates of the wind shear (division of CTL–CTMSL) and TKE or temperature gradient (division of TISL–FT), we disregard the division points detected too close to the local extremum of the aircraft altitude. More detail can be seen in [Jen-La Plante et al. \(2016\)](#).

1) POWER SPECTRA ANALYSIS

The ensemble-averaged spectra of T and LWC for the sublayers of MSC top region are also shown in [Fig. 3](#). The scaling regimes for T and LWC at the sublayers are similar with that for the horizontal segments in the STBL, with two distinct scaling regimes, but the scale invariance of large-scale regime breaks at higher frequencies (smaller scales) and with higher values of β_L . For LWC, the first scaling regime breaks at about 0.76 m with $\beta_L = 1.58$ for CTMSL and breaks at 1.04 m with $\beta_L = 1.57$ for CTL. The second scaling regime is in the range of 0.22 – 0.76 m at CTMSL with $\beta_S = 0.77$ and 0.37 – 1.04 m at CTL with $\beta_S = 0.76$. For temperature, the large-scale regime breaks at about 0.64 , 0.13 , 0.18 , and 0.36 m for FT, TISL, CTMSL, and CTL, respectively, with $\beta_L = 1.84$, 1.84 , 1.82 , and 1.69 . The small-scale regime is in the range from 0.11 – 0.13 to 0.64 m, with β_S close to 1 , most likely indicating that the viscous–convective subrange exists in the cloud-top region.

2) STRUCTURE FUNCTION ANALYSIS

We also checked the scaling behavior of T and LWC for these sublayers of MSC top region using structure function analysis. The results are shown in [Table 4](#). We find that $\zeta(1)$ and $\zeta(2)$ for both T and LWC increase with altitude within cloud-top region. For temperature, the largest value of $\zeta(1)$ appears at FT, indicating that temperature records are more smooth, which is consistent with the measured properties of the FT that [Malinowski et al. \(2013\)](#) described. The rapid transition of scaling exponents from $\zeta(1) \approx 1/3$ in the cloud mixed layer to $\zeta(1) > 1/2$ in the free troposphere seems to support the hypothesized role of buoyant convective motions in establishing the convective mixed layer spectra over relatively short time ([Fischer et al. 2012, 2013; Pressel et al. 2014](#)). The value of $\zeta(1)$ for LWC (0.28) at CTMSL is close to $1/3$, which is the same as that in FIRE and ASTEX ([Marshak et al. 1997](#)). But, it is slightly smaller at CTL. For the parameter ζ_∞ , the smallest value occurs at CTMSL and the biggest value appears at FT, indicating that T and LWC fluctuations

of MSC top region are more intermittent at CTMSL and less intermittent at FT.

4. Discussion

a. Vertical structure of scaling exponents within STBL

Comparing all layers from near sea surface to free atmosphere, we find that the scale break; scaling exponents β , $\zeta(1)$, and $\zeta(2)$; and intermittency parameter $1/\zeta_\infty$ for the large scale significantly vary with height in STBL, especially in the MSC top region (see [Fig. 6](#)). The ensemble-mean scaling parameters are calculated by two different averaging methods, and the results are consistent. The scale break for LWC decreases from ~ 5 m at hCB to 0.8 m at CTMSL. For temperature, it decreases from ~ 5 m at hNS to 0.13 m at TISL and then increases to 0.6 m at FT and ~ 2.2 m at hFA (which is higher than FT, and is not shown in [Fig. 6](#)). The spectral exponent β of temperature is lower than $5/3$ under the cloud-top region and distinctly increases with height within STBL top region with a value larger than $5/3$. The β of LWC increases with height in the cloud and is close to $5/3$ at cloud-top layer. This feature of β for T and LWC for the large-scale regime is similar to the behavior of β for water vapor increasing with height in the free troposphere and it is larger than that in the boundary layer (BL) detected from satellite ([Kahn et al. 2011](#)), aircraft ([Cho et al. 2000; Kahn et al. 2011](#)), and tower ([Pressel et al. 2014](#)) measurements.

The scaling exponents $\zeta(1)$ and $\zeta(2)$ for T and LWC show similar features to the spectral exponent β . For LWC, $\zeta(1)$ increases from 0.12 at hCB to 0.28 at CTMSL. For T , the values of $\zeta(1)$ are close to Kolmogorov theoretical value $1/3$ below CTL, then increase sharply within cloud-top region and reach maximum 0.52 at FT. The values of $\zeta(2) + 1$ are consistent with β calculated from spectra, but they are systematically a little smaller than β within STBL. This difference may be attributed to the limitation of the Wiener–Khinchin theorem (it is only valid for stationary fields or non-stationary fields with stationary increments) and to the uncertainty of fitting technique. From the intermittency parameter $1/\zeta_\infty$, we easily can see higher intermittency in the cloud-top region below TISL and less intermittency in the free atmosphere and near sea surface. In addition, the values of β , $\zeta(1)$, and $\zeta(2)$ for LWC are obviously smaller than that for T within STBL. This indicates that the LWC records are rougher than those of T , as shown by the measurements of LWC, which have many strong down spikes related to the cloud holes ([Gerber et al. 2005](#)). This spikiness (concentrated energy at small

TABLE 4. Characteristics and statistical properties for the different sublayers of MSC top region during POST. The quantity N_{sub} is the number of independent nonoverlapping subsegments separated from individual penetration segments with 2^{11} sampling points, corresponding to ~ 112.6 m. For LWC, $N_{\text{sub}} = 2742$ at CTMSL and $N_{\text{sub}} = 875$ at CTL.

Layer	N_{sub}	z (m)	T ($^{\circ}\text{C}$)	LWC (g m^{-3})	Scaling exponents of T				Scaling exponents of LWC			
					β	$\zeta(1)$	$\zeta(2)$	ζ_{∞}	β	$\zeta(1)$	$\zeta(2)$	ζ_{∞}
FT	1318	630 ± 97	18.2 ± 3.5	0	1.84 ± 0.02	0.52 ± 0.04	0.92 ± 0.05	2.12 ± 0.17				
TISL	1696	585 ± 100	15.1 ± 2.1	0	1.84 ± 0.01	0.49 ± 0.02	0.82 ± 0.03	1.87 ± 0.08				
CTMSL	3213	542 ± 105	10.7 ± 0.9	0.252 ± 0.068	1.82 ± 0.01	0.41 ± 0.004	0.68 ± 0.002	0.74 ± 0.08	1.58 ± 0.01	0.28 ± 0.003	0.50 ± 0.02	1.05 ± 0.07
CTL	891	479 ± 108	10.6 ± 1.0	0.324 ± 0.077	1.69 ± 0.02	0.30 ± 0.003	0.55 ± 0.01	1.16 ± 0.14	1.57 ± 0.01	0.20 ± 0.004	0.41 ± 0.02	1.11 ± 0.11

scales) yield a smaller β than the smoother signal (more energy in the mean and large scales) (Davis et al. 1996b) and also result in a smaller $\zeta(1)$ and $\zeta(2)$ (Marshak et al. 1997). In addition, the scaling parameters of LWC probably depend on the concentration and size of droplets.

We conclude that the spatial scale break decreases with height in STBL with the minimum at the EIL (the interface between cloud and the free atmosphere). This feature can be related to the clouds' filamentary structure in the cloud-top region. The entrainment, mixing and evaporation processes in the EIL result in the formation of filaments of cloudy and clear air at different stages of stirring, mixing, and homogenization with sizes smaller than centimeters in this interface layer (Haman et al. 2007); the closer to the interface, the smaller the structure size. Thus, the scale invariance usually breaks at the smallest scale at the EIL, then the scale break increases farther from the interface. We further conclude that the scaling exponents β , $\zeta(1)$, and $\zeta(2)$ increase with height in STBL and their values are larger than the Kolmogorov theoretical values [$\beta = 5/3$, $\zeta(1) = 1/3$, and $\zeta(2) = 2/3$] within MSC top region. This feature is likely affected by the wave-turbulence interaction and the anisotropic eddies produced by wind shear present across the inversion layer (Pedersen et al. 2016; Kopec et al. 2016). The wind shear and stable stratification make the turbulence in both sublayers TISL and CTMSL highly anisotropic (Jen-La Plante et al. 2016); thus, in the region around cloud top, the anisotropic turbulence shows anomalous scaling behavior with larger scaling exponents than for isotropic turbulence (Biferale et al. 2004). In addition, the intermittency parameter $1/\zeta_{\infty}$ increases with height and reaches the maximum at CTMSL, then decreases toward the FT. The strong intermittency of T and LWC fluctuations in the cloud-top region (below TISL) is most likely caused by the entrainment and evaporation processes.

b. Bifractal properties of STBL and MSC structure

To characterize the basic scale-invariant properties (nonstationarity and intermittency) for atmospheric T and LWC signals in STBL and MSC, we calculate H_1 (measures the nonstationarity) and C_1 (measures the intermittency). For convenience we use the following formulas from Davis et al. (1999) to estimate these two important parameters of multifractals:

$$H_1 = a\zeta_{\infty}/(a + \zeta_{\infty}) \quad \text{and} \quad (5)$$

$$C_1 = \zeta_{\infty}/(\zeta_{\infty}/a + 1)^2, \quad (6)$$

where a and ζ_{∞} are two parameters of the **Pierrehumbert** (1996) parameterization [Eq. (4)]. The values of H_1 estimated from Eq. (5) are consistent with $\zeta(1)$, with the

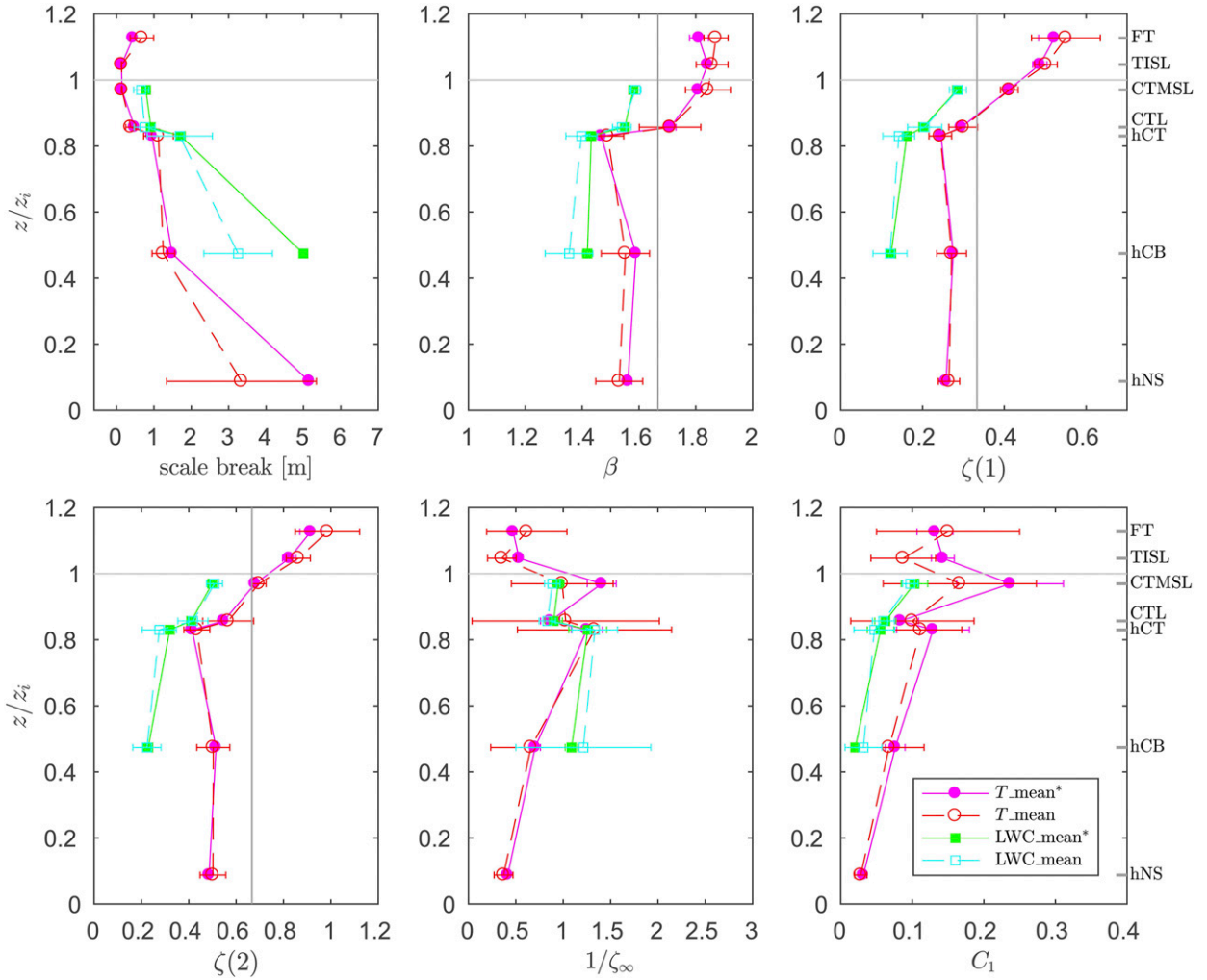


FIG. 6. Ensemble-mean scaling exponents β , $\zeta(1)$, and $\zeta(2)$, intermittency parameter $1/\zeta_\infty$, and C_1 , as well as scale break for the inertial subrange of T and LWC fluctuations in the STBL vs the normalized height (z/z_i) or layers from six flights during POST campaign. The quantity $z_i \simeq 566$ m is the mean cloud-top height. The pink dots and red circles with clear centers are for T , and the green squares and cyan squares with clear centers are for LWC. The word mean is the traditional arithmetic average from all individual spectra or structure function of each segment, and mean* is calculated from the aggregated spectra or structure function. The error bars for mean are standard deviations and for mean* are 95% confidence intervals. The horizontal gray line is cloud top and vertical gray lines are $\beta = 5/3$, $\zeta(1) = 1/3$, and $\zeta(2) = 2/3$.

differences usually less than 0.02. The comparison with singularity analysis by Davis et al. (1999) indicated a little larger dispersion of (H_1, C_1) points in the bifractal plane using this method, especially along the C_1 axis, but it did not change the final conclusions. Therefore, this simple method is suitable.

Figure 7 shows a (H_1, C_1) scatterplot for T and LWC fluctuations for the scales larger than 1–5 m. In the main panel the points are the ensemble mean (H_1, C_1) for each layer calculated from the aggregated structure function of all six flights. The uncertainties are estimated at the 95% confidence level by substituting the

uncertainties of a and ζ_∞ into Eqs. (5) and (6). In the inset panels the points are mean values for each layer of every flight; that is, each layer has six points with same color. All the points fall inside the box, and none of them fall on the axes. Following the conclusion of Marshak et al. (1997) and Davis et al. (1999), we argue that this feature indicates that the standard scale-invariant stochastic models, such as fractional Brownian motion (fBm; nonstationary but nonintermittent), multiplicative cascade models (intermittent but stationary), random devil's staircases (too smooth), and isolated singularities (too intermittent) are not enough

to represent either turbulent T or LWC in STBL and MSC. Instead hybrid stochastic models with both non-stationary (additive) and intermittent (multiplicative) features are needed for description of T and LWC fields in STBL and MSC. From POST data we get the ensemble averages (H_1 , C_1) of LWC in a wider range ($0.14 \leq H_1 \leq 0.33$, $0.02 \leq C_1 \leq 0.10$) in comparison to the mean values ($0.28 \leq H_1 \leq 0.31$, $0.08 \leq C_1 \leq 0.12$) of other MSC (ASTEX, FIRE, and SOCEX) (Davis et al. 1999). This wide range is mainly due to our fine-layered division. We also get the mean values of (H_1 , C_1) for T : ($0.28 \leq H_1 \leq 0.53$, $0.03 \leq C_1 \leq 0.24$) in the STBL and ($0.31 \leq H_1 \leq 0.52$, $0.08 \leq C_1 \leq 0.24$) in MSC. This range is also larger than the mean value of passive scalars in turbulence (Marshak et al. 1997; Davis et al. 1999).

For POST MSC the mean values of (H_1 , C_1) are (0.23, 0.06) for LWC and (0.32, 0.09) for T . The former is close to that for LWC in other MSC: (0.28, 0.10) in FIRE, (0.29, 0.08) in ASTEX, and (0.31, 0.12) in SOCEX (Marshak et al. 1997; Davis et al. 1999), and the latter also fall in the region of passive scalars in turbulence in the Fig. 13 of Marshak et al. (1997) and Fig. 8 of Davis et al. (1999). This confirms the conclusion from Marshak et al. (1997) and Davis et al. (1999) that the internal structures of MSC are essentially “universal.” It means the local climate seems to determine primarily the range of scales (cf. our Table 2 and Table 1 in Davis et al. 1999) but does not determine the two important scaling exponents (Davis et al. 1999).

However, the past studies did not analyze the vertical structure of these two multifractal parameters. In comparison with the past studies, we obtain more details from our fine-layered division. We find that both C_1 and H_1 increase with height from near the sea surface to cloud top (the top of CTMSL) (also see Fig. 6) and C_1 increases with H_1 below the cloud top. From cloud base to cloud top LWC exhibits a statistically significant linear relationship $C_1 \approx 0.4H_1 - 0.04$ ($p < 0.025$ for the ensemble mean and $p < 0.005$ for the individual flights). For T , we see the same feature that C_1 increases with H_1 and height from hNS to CTMSL, with a significant linear relationship $C_1 \approx 1.5H_1 - 0.39$ ($p < 0.025$ and $p < 0.01$ for the ensemble mean and individual flights, respectively). However, the points in the top-right panel are more scattered, which calls for more datasets to be investigated. In thin layers (TISL and FT) above the cloud-top H_1 increases with height and C_1 sharply decreases with height. This means that the intermittency diminishes quickly and nonstationarity increases from the cloud top to the free atmosphere. The smallest value of C_1 can be found in the hFA as expected. This result confirms again that the current standard scale-invariant stochastic models are

not enough to represent the turbulence in the STBL and MSC and that a more complex integrated stochastic model is needed. Such a model should account for both intermittency and nonstationarity, their height dependence, as well as the relationship between them. In particular, our analysis indicates that three different turbulent regimes located near the sea surface, in the middle of boundary layer, and in the cloud-top region should be distinguished.

5. Conclusions

We have shown that from near sea surface to cloud top both T and LWC of POST data have two distinct scaling regimes, similar to the scaling behavior of LWC presented by Davis et al. (1996b, 1999). One regime is scale invariant over a range from 1–5 m to at least 7 km, and the other goes from about 0.1–1 to 1–5 m depending on height and variable. For the large scales ($r > 1$ –5 m), we obtain the following conclusions:

- 1) The scale break and scaling exponents β , $\zeta(1)$, and $\zeta(2)$ for both T and LWC fluctuations vary with height in STBL, especially in the MSC top region. The scale break (in length scale) increases from the EIL to near the sea surface and the free atmosphere. The values of scaling exponents for T are somewhat smaller than the theoretical values [$\beta = 5/3$, $\zeta(1) = 1/3$, and $\zeta(2) = 2/3$] for nonintermittent isotropic turbulence below the cloud top and slightly larger than the theoretical values in the upper part of STBL top region with the maxima at FT. These values for LWC are significantly smaller than those for T . The values of $\beta/\zeta(1)$ increase from 1.49/0.26 near the sea surface to 1.84/0.52 at the free atmosphere for T and increase from 1.42/0.12 at cloud base to 1.58/0.28 at cloud top for LWC. Within MSC, T and LWC time series are less smooth but more stationary near cloud base and are less rough but more nonstationary near cloud top.
- 2) From the intermittency parameter $1/\zeta_\infty$ we find that the signals of temperature are strongly intermittent in cloud and weakly intermittent in the free atmosphere. In MSC, the maximum intermittency occurs within the cloud-top region (usually at the sublayer CTMSL) for both T and LWC fluctuations.
- 3) The scattered nature of bifractal properties (H_1 , C_1) confirms that the standard scale-invariant stochastic models are not enough to represent the internal structure of atmospheric turbulence in the STBL and MSC, and a more complex integrated stochastic model is needed. In addition, our analysis of the fine-layered division of the cloud top and capping

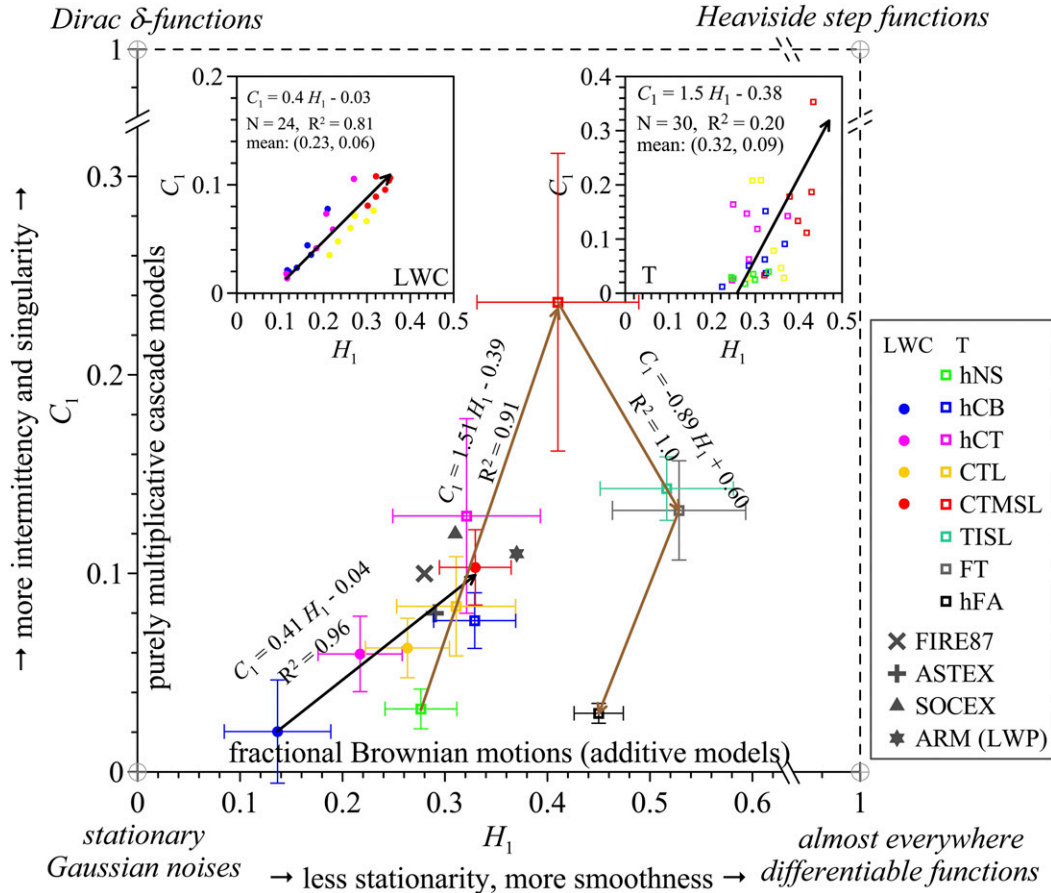


FIG. 7. Scale-invariant properties of POST STBL turbulence in the bifractal plane. The index of non-stationarity (smoothness of data) H_1 increases horizontally, and the index of intermittency (sparseness of large jumps in data) C_1 increases vertically. The horizontal axis is host to nonstationary and nonintermittent additive models (fractional Brownian motions) and the vertical axis to intermittent and stationary multiplicative cascade models. The four corners of the large domain are occupied by four well-known cases. The solid and clear markers are respectively for LWC and T of POST, and the layers and sublayers are distinguished by colors. The error bars are the 95% confidence intervals. Arrow lines are linear fitting for LWC and T in different regions (from hNS to CTMSL, CTMSL to FT, and FT to hFA). The main panel is ensemble-mean (H_1 , C_1) of all flights, and the inset small panels are scatterplots of H_1 and C_1 for (left) LWC and (right) T of all layers and sublayers from hNS to CTMSL from each individual flight. The mean values of other MSC LWC in FIRE, ASTEX, SOCEX, and liquid water path (LWP) in ARM from Marshak et al. (1997) and Davis et al. (1999) are also added in the figure.

inversion shows that the bifractal parameters (H_1 , C_1) for both T and LWC vary with height in the STBL. For LWC, they increase from (0.14, 0.02) at cloud base to (0.33, 0.1) at cloud top, while maintaining a statistically significant linear relationship $C_1 \approx 0.4H_1 - 0.04$ in MSC. Temperature displays similar behavior from near surface to cloud top, but above it H_1 increases and C_1 decreases with height. Our findings suggest that three different turbulence regimes (near the sea surface, middle of the boundary layer, and cloud-top region) in the STBL need to be considered.

This paper shows the scaling behavior of MSC is more complex than that implied from the previous studies. The different multifractal behavior of various observed layers within stratocumulus clouds is useful for improved parameterization of subgrid-scale effects in numerical models. The different scaling behavior of T and LWC across the STBL from that in the CTMSL and TISL calls for separate treatment of turbulent transport across the convective STBL and the exchange across the inversion between BL and troposphere. This is supported with the findings of Malinowski et al. (2013) and Jen-La Plante et al. (2016).

The organization of large-scale cloud convection and turbulence in BL and entrainment into BL across the inversion should be treated as different processes in numerical models. The reliability of our conclusions described here would benefit from the investigation of additional datasets.

Acknowledgments. POST experiment was supported by the National Science Foundation under Grant ATM-0735121 and the Polish Ministry of Science and Higher Education under Grant 186/W-POST/2008/0. The present analysis was supported by the Polish National Science Center under Grant DEC-2013/08/A/ST10/00291. We are grateful to four anonymous reviewers for their insightful and constructive reviews.

APPENDIX A

List of Abbreviations and Acronyms

ARM	Atmospheric Radiation Measurement Program
ASTEX	Atlantic Stratocumulus Transition Experiment
Cu	Cumulus
EIL	Entrainment interfacial layer
fBm	Fractional Brownian motion
FIRE	First ISCCP Research Experiment
LSM	Least squares method
LWP	Liquid water path
MBL	Marine boundary layer
MC	Monte Carlo
MSC	Marine stratocumulus clouds
NASA	National Aeronautics and Space Administration
POST	Physics of Stratocumulus Top
PVM	Particulate volume monitor
Sc	Stratocumulus
SOCEX	Southern Ocean Cloud Experiment
STBL	Stratocumulus-topped boundary layer
TKE	Turbulence kinetic energy
TO	Twin Otter (name of the aircraft)
UFT-M	Modified UltraFast Thermometer
VOCALS-REx	Variability of the American Monsoon Systems Ocean-Cloud-Atmosphere-Land Study Regional Experiment

APPENDIX B

Layers Grouped from Horizontal Segments

hFA	Free-atmosphere layer
hCT	Cloud-top layer (in the cloud close to the cloud top)

hCB	Cloud-base layer
hNS	Near-sea surface layer

APPENDIX C

Sublayers in the Cloud-Top Region Grouped from Porpoises

FT	Free troposphere
TISL	Turbulent inversion sublayer
CTMSL	Cloud-top mixing sublayer
CTL	Cloud-top layer

APPENDIX D

List of Parameters

z	Altitude
T	Temperature
LWC	Liquid water content
a	A parameter of roughness after Pierrehumbert (1996)
β	Spectral exponent
β_L/β_S	β of large/small scale
$\Delta\beta$	Uncertainty of β
C_1	Intermittency parameter
H_1	Nonstationarity parameter (Hurst exponent or roughness)
SR_L/SR_S	Scale range of large/small scale
$\xi(1)$	Exponent of the first-order structure function
$\xi(2)$	Exponent of the second-order structure function
$\xi(q)$	Exponent of the q th-order structure function
ξ_∞	Intermittency parameter after Pierrehumbert (1996)

REFERENCES

- Albrecht, B. A., D. A. Randall, and S. Nicholls, 1988: Observations of marine stratocumulus clouds during FIRE. *Bull. Amer. Meteor. Soc.*, **69**, 618–626, [https://doi.org/10.1175/1520-0477\(1988\)069<0618:OOMSCD>2.0.CO;2](https://doi.org/10.1175/1520-0477(1988)069<0618:OOMSCD>2.0.CO;2).
- , C. S. Bretherton, D. Johnson, W. H. Schubert, and A. S. Frisch, 1995: The Atlantic Stratocumulus Transition Experiment—ASTEX. *Bull. Amer. Meteor. Soc.*, **76**, 889–904, [https://doi.org/10.1175/1520-0477\(1995\)076<0889:TASTE>2.0.CO;2](https://doi.org/10.1175/1520-0477(1995)076<0889:TASTE>2.0.CO;2).
- Batchelor, G. K., 1959: Small-scale variation of convected quantities like temperature in turbulent fluid. Part I: General discussion and the case of small conductivity. *J. Fluid Mech.*, **5**, 113–133, <https://doi.org/10.1017/S002211205900009X>.
- Berton, R. P. H., 2008: Analysis of physical parameters measured during the ECRIN 96 Experiment. *Atmos. Res.*, **89**, 30–47, <https://doi.org/10.1016/j.atmosres.2007.09.008>.

- Biferale, L., I. Daumont, A. Lanotte, and F. Toschi, 2004: Theoretical and numerical study of highly anisotropic turbulent flows. *Eur. J. Mech.*, **23B**, 401–414, <https://doi.org/10.1016/j.euromechflu.2003.10.010>.
- Boers, R., J. B. Jensen, P. B. Krummel, and H. Gerber, 1996: Microphysical and short-wave radiative structure of wintertime stratocumulus clouds over the Southern Ocean. *Quart. J. Roy. Meteor. Soc.*, **122**, 1307–1339, <https://doi.org/10.1002/qj.49712253405>.
- Cahalan, R. F., 1994: Bounded cascade clouds: Albedo and effective thickness. *Nonlinear Processes Geophys.*, **1**, 156–167, <https://doi.org/10.5194/npg-1-156-1994>.
- Carman, J. K., D. L. Rossiter, D. Khelif, H. H. Jonsson, I. C. Faloona, and P. Y. Chuang, 2012: Observational constraints on entrainment and the entrainment interface layer in stratocumulus. *Atmos. Chem. Phys.*, **12**, 11 135–11 152, <https://doi.org/10.5194/acp-12-11135-2012>.
- Celani, A., M. Cencini, M. Vergassola, E. Villermaux, and D. Vincenzi, 2005: Shear effects on passive scalar spectra. *J. Fluid Mech.*, **523**, 99–108, <https://doi.org/10.1017/S0022112004002332>.
- Cess, R. D., and Coauthors, 1989: Interpretation of cloud-climate feedback as produced by 14 atmospheric general circulation models. *Science*, **245**, 513–516, <https://doi.org/10.1126/science.245.4917.513>.
- Cho, J. Y. N., R. E. Newell, and J. D. Barrick, 1999: Horizontal wavenumber spectra of winds, temperature, and trace gases during the Pacific Exploratory Missions. 2. Gravity waves, quasi-two-dimensional turbulence, and vertical modes. *J. Geophys. Res.*, **104**, 16 297–16 308, <https://doi.org/10.1029/1999JD900068>.
- , —, and G. W. Sachse, 2000: Anomalous scaling of mesoscale tropospheric humidity fluctuations. *Geophys. Res. Lett.*, **27**, 377–380, <https://doi.org/10.1029/1999GL010846>.
- Davidson, P. A., Y. Kaneda, and K. R. Sreenivasan, 2012: *Ten Chapters in Turbulence*. Cambridge University Press, 437 pp., doi:10.1017/CBO9781139032810.
- Davis, A., A. Marshak, W. Wiscombe, and R. Cahalan, 1994: Multifractal characterizations of nonstationarity and intermittency in geophysical fields: Observed, retrieved, or simulated. *J. Geophys. Res.*, **99**, 8055–8072, <https://doi.org/10.1029/94JD00219>.
- , —, —, and —, 1996a: Multifractal characterizations of intermittency in nonstationary geophysical signals and fields: A model-based perspective on ergodicity issues illustrated with cloud data. *Current Topics in Nonstationary Analysis*, G. Treviño et al., Eds., World Scientific, 97–158.
- , —, —, and —, 1996b: Scale invariance of liquid water distributions in marine stratocumulus. Part I: Spectral properties and stationarity issues. *J. Atmos. Sci.*, **53**, 1538–1558, [https://doi.org/10.1175/1520-0469\(1996\)053<1538:SIOLWD>2.0.CO;2](https://doi.org/10.1175/1520-0469(1996)053<1538:SIOLWD>2.0.CO;2).
- , —, R. Cahalan, and W. Wiscombe, 1997: The Landsat scale break in stratocumulus as a three-dimensional radiative transfer effect: Implications for cloud remote sensing. *J. Atmos. Sci.*, **54**, 241–260, [https://doi.org/10.1175/1520-0469\(1997\)054<0241:TLSBIS>2.0.CO;2](https://doi.org/10.1175/1520-0469(1997)054<0241:TLSBIS>2.0.CO;2).
- , —, H. Gerber, and W. J. Wiscombe, 1999: Horizontal structure of marine boundary layer clouds from centimeter to kilometer scales. *J. Geophys. Res.*, **104**, 6123–6144, <https://doi.org/10.1029/1998JD200078>.
- Fallah, B., A. A. Saberi, and S. Sodoudi, 2016: Emergence of global scaling behaviour in the coupled Earth-atmosphere interaction. *Sci. Rep.*, **6**, 34 005, <https://doi.org/10.1038/srep34005>.
- Fischer, L., C. Kiemle, and G. C. Craig, 2012: Height-resolved variability of midlatitude tropospheric water vapor measured by an airborne lidar. *Geophys. Res. Lett.*, **39**, L06803, <https://doi.org/10.1029/2011GL050621>.
- , G. C. Craig, and C. Kiemle, 2013: Horizontal structure function and vertical correlation analysis of mesoscale water vapor variability observed by airborne lidar. *J. Geophys. Res. Atmos.*, **118**, 7579–7590, <https://doi.org/10.1002/jgrd.50588>.
- Gerber, H., B. G. Arends, and A. S. Ackerman, 1994: New microphysics sensor for aircraft use. *Atmos. Res.*, **31**, 235–252, [https://doi.org/10.1016/0169-8095\(94\)90001-9](https://doi.org/10.1016/0169-8095(94)90001-9).
- , J. B. Jensen, A. B. Davis, A. Marshak, and W. J. Wiscombe, 2001: Spectral density of cloud liquid water content at high frequencies. *J. Atmos. Sci.*, **58**, 497–503, [https://doi.org/10.1175/1520-0469\(2001\)058<0497:SDOCLW>2.0.CO;2](https://doi.org/10.1175/1520-0469(2001)058<0497:SDOCLW>2.0.CO;2).
- , G. Frick, S. Malinowski, J. Brenguier, and F. Burnet, 2005: Holes and entrainment in stratocumulus. *J. Atmos. Sci.*, **62**, 443–459, <https://doi.org/10.1175/JAS-3399.1>.
- , —, —, W. Kumula, and S. Krueger, 2010: POST—A new look at stratocumulus. *13th Conf. on Cloud Physics*, Portland, OR, Amer. Meteor. Soc., 10.1, https://ams.confex.com/ams/13CldPhy13AtRad/techprogram/paper_170431.htm.
- , —, —, H. Jonsson, D. Khelif, and S. K. Krueger, 2013: Entrainment rates and microphysics in POST stratocumulus. *J. Geophys. Res. Atmos.*, **118**, 12 094–12 109, <https://doi.org/10.1002/jgrd.50878>.
- Gibson, C. H., and W. H. Schwarz, 1963: The universal equilibrium spectra of turbulent velocity and scalar fields. *J. Fluid Mech.*, **16**, 365–384, <https://doi.org/10.1017/S0022112063000835>.
- Grant, H. L., B. A. Hughes, W. M. Vogel, and A. Moilliet, 1968: The spectrum of temperature fluctuations in turbulent flow. *J. Fluid Mech.*, **34**, 423–442, <https://doi.org/10.1017/S0022112068001990>.
- Haman, K. E., S. P. Malinowski, M. J. Kurowski, H. Gerber, and J.-L. Brenguier, 2007: Small scale mixing processes at the top of a marine stratocumulus—A case study. *Quart. J. Roy. Meteor. Soc.*, **133**, 213–226, <https://doi.org/10.1002/qj.5>.
- Hill, R. J., 1989: Structure functions and spectra of scalar quantities in the inertial-convective and viscous-convective ranges of turbulence. *J. Atmos. Sci.*, **46**, 2245–2251, [https://doi.org/10.1175/1520-0469\(1989\)046<2245:SFAOS>2.0.CO;2](https://doi.org/10.1175/1520-0469(1989)046<2245:SFAOS>2.0.CO;2).
- Jeffery, C. A., 2001: Effect of condensation and evaporation on the viscous-convective subrange. *Phys. Fluids*, **13**, 713–722, <https://doi.org/10.1063/1.1343481>.
- Jen-La Plante, I., and Coauthors, 2016: Physics of Stratocumulus Top (POST): Turbulence characteristics. *Atmos. Chem. Phys.*, **16**, 9711–9725, <https://doi.org/10.5194/acp-16-9711-2016>.
- Kahn, B. H., and Coauthors, 2011: Temperature and water vapor variance scaling in global models: Comparisons to satellite and aircraft data. *J. Atmos. Sci.*, **68**, 2156–2168, <https://doi.org/10.1175/2011JAS3737.1>.
- Kopec, M. K., S. P. Malinowski, and Z. P. Piotrowski, 2016: Effects of wind shear and radiative cooling on the stratocumulus-topped boundary layer. *Quart. J. Roy. Meteor. Soc.*, **142**, 3222–3233, <https://doi.org/10.1002/qj.2903>.
- Kumala, W., K. E. Haman, M. K. Kopec, D. Khelif, and S. P. Malinowski, 2013: Modified ultrafast thermometer UFT-M and temperature measurements during Physics of Stratocumulus Top (POST). *Atmos. Meas. Tech.*, **6**, 2043–2054, <https://doi.org/10.5194/amt-6-2043-2013>.
- Kundu, P. K., I. M. Cohen, P. S. Ayyaswamy, and H. H. Hu, 2008: *Fluid Mechanics*. Academic Press, 872 pp.

- Malinowski, S. P., M. Y. Leclerc, and D. G. Baumgardner, 1994: Fractal analyses of high-resolution cloud droplet measurements. *J. Atmos. Sci.*, **51**, 397–413, [https://doi.org/10.1175/1520-0469\(1994\)051<0397:FAOHRC>2.0.CO;2](https://doi.org/10.1175/1520-0469(1994)051<0397:FAOHRC>2.0.CO;2).
- , M. Andrejczuk, W. W. Grabowski, P. Korczyk, T. A. Kowalewski, and P. K. Smolarkiewicz, 2008: Laboratory and modeling studies of cloud–clear air interfacial mixing: Anisotropy of small-scale turbulence due to evaporative cooling. *New J. Phys.*, **10**, 075020, <https://doi.org/10.1088/1367-2630/10/7/075020>.
- , and Coauthors, 2013: Physics of Stratocumulus Top (POST): Turbulent mixing across capping inversion. *Atmos. Chem. Phys.*, **13**, 12 171–12 186, <https://doi.org/10.5194/acp-13-12171-2013>.
- Marshak, A., A. Davis, W. Wiscombe, and R. Cahalan, 1997: Scale invariance in liquid water distributions in marine stratocumulus. Part II: Multifractal properties and intermittency issues. *J. Atmos. Sci.*, **54**, 1423–1444, [https://doi.org/10.1175/1520-0469\(1997\)054<1423:SIILWD>2.0.CO;2](https://doi.org/10.1175/1520-0469(1997)054<1423:SIILWD>2.0.CO;2).
- Monin, A. S., and A. M. Yaglom, 1975: *Statistical Fluid Mechanics: Mechanics of Turbulence*. MIT Press, 874 pp.
- Pedersen, J. G., S. P. Malinowski, and W. W. Grabowski, 2016: Resolution and domain-size sensitivity in implicit large-eddy simulation of the stratocumulus-topped boundary layer. *J. Adv. Model. Earth Syst.*, **8**, 885–903, <https://doi.org/10.1002/2015MS000572>.
- Pierrehumbert, R. T., 1996: Anomalous scaling of high cloud variability in the tropical Pacific. *Geophys. Res. Lett.*, **23**, 1095–1098, <https://doi.org/10.1029/96GL01121>.
- Pressel, K. G., W. D. Collins, and A. R. Desai, 2014: The spatial scale dependence of water vapor variability inferred from observations from a very tall tower. *J. Geophys. Res. Atmos.*, **119**, 9822–9837, doi:[10.1002/2013JD021141](https://doi.org/10.1002/2013JD021141).
- Ramanathan, V., R. D. Cess, E. F. Harrison, P. Minnis, B. R. Barkstrom, E. Ahmad, and D. Hartmann, 1989: Cloud-radiative forcing and climate: Results from the Earth Radiation Budget Experiment. *Science*, **243**, 57–63, <https://doi.org/10.1126/science.243.4887.57>.
- Riley, J. J., and E. Lindborg, 2008: Stratified turbulence: A possible interpretation of some geophysical turbulence measurements. *J. Atmos. Sci.*, **65**, 2416–2424, <https://doi.org/10.1175/2007JAS2455.1>.
- Smyth, W. D., and J. N. Moum, 2009: Three-dimensional (3D) turbulence. *Elements of Physical Oceanography: A Derivative of the Encyclopedia of Ocean Sciences*, J. Steele, S. Thorpe, and K. Turekian, Eds., Academic Press, 367–374.
- Stanfield, R. E., X. Dong, B. Xi, A. Kennedy, A. D. Del Genio, P. Minnis, and J. H. Jiang, 2014: Assessment of NASA GISS CMIP5 and post-CMIP5 simulated clouds and TOA radiation budgets using satellite observations. Part I: Cloud fraction and properties. *J. Climate*, **27**, 4189–4208, <https://doi.org/10.1175/JCLI-D-13-00558.1>.
- Sukoriansky, S., and B. Galperin, 2013: An analytical theory of the buoyancy–Kolmogorov subrange transition in turbulent flows with stable stratification. *Philos. Trans. Roy. Soc. London*, **A371**, 20120212, doi:[10.1098/rsta.2012.0212](https://doi.org/10.1098/rsta.2012.0212).
- Tuck, A. F., 2010: From molecules to meteorology via turbulent scale invariance. *Quart. J. Roy. Meteor. Soc.*, **136**, 1125–1144, <https://doi.org/10.1002/qj.644>.
- Willis, G. E., and J. W. Deardorff, 1974: A laboratory model of the unstable planetary boundary layer. *J. Atmos. Sci.*, **31**, 1297–1307, [https://doi.org/10.1175/1520-0469\(1974\)031<1297:ALMOTU>2.0.CO;2](https://doi.org/10.1175/1520-0469(1974)031<1297:ALMOTU>2.0.CO;2).
- Wood, R., 2012: Stratocumulus clouds. *Mon. Wea. Rev.*, **140**, 2373–2423, <https://doi.org/10.1175/MWR-D-11-00121.1>.